Magnetoelastic coupling in $La_{0.7}Ca_{0.3}MnO_3/BaTiO_3$ ultrathin films

A. Alberca,[1,5] N. M. Nemes,[2,5] F. J. Mompean,[1,5] T. Fehér,[4] F. Simon,[4] J. Tornos,[2,5] C. Leon,[2,5] C. Munuera,[1,5]
B. J. Kirby,[6] M. R. Fitzsimmons,[7] A. Hernando,[3] J. Santamaria,[2,5] and M. Garcia-Hernandez[1,5]

[1]*Instituto de Ciencia de Materiales de Madrid, Consejo Superior de Investigaciones Científicas, Sor Juana Inés de la Cruz, 3, ES-28049 Madrid, Spain*

[2]*Departamento de Física Aplicada III, Universidad Complutense, Ciudad Universitaria, ES-28040 Madrid, Spain*

[3]*Departamento de Física de Materiales and Instituto de Magnetismo Aplicado "Salvador Velayos," Universidad Complutense, Ciudad Universitaria, ES-28040 Madrid, Spain*

[4]*Department of Physics, Budapest University of Technology and Economics and Condensed Matter Research Group of the Hungarian Academy of Sciences, Budafoki ut 8., H-1111 Budapest, Hungary*

[5]*Laboratorio de Heteroestructuras con aplicación en Spintronica, Unidad Asociada Consejo Superior de Investigaciones Científicas/ Universidad Complutense Madrid, Sor Juana Inés de la Cruz, 3, ES-28049 Madrid, Spain*

[6]*Center for Neutron Research, National Institute of Standards and Technology, Gaithersburg, Maryland 20899, USA*

[7]*Los Alamos National Laboratory, Los Alamos, New Mexico 87545, USA*

(Received 8 May 2013; revised manuscript received 23 July 2013; published 11 October 2013)

The magnetism of $La_{0.7}Ca_{0.3}MnO_3$ (LCMO) epitaxial thin films grown on $SrTiO_3$ (STO) and $BaTiO_3$ (BTO) substrates is studied using polarized neutron reflectometry (PNR) and ferromagnetic resonance (FMR) techniques. In LCMO/BTO, PNR reveals a strongly suppressed magnetization of 300 kA/m, equivalent to a magnetic moment of 2 μB/Mn, throughout the LCMO layer, amounting to half the expected value. The largest suppression occurs near the interface with BTO, with magnetization values of 50 kA/m, equivalent to 0.3 μB/Mn. FMR is observable at 8.9 GHz only around the [110] crystallographic direction in thin LCMO/BTO. The resonance barely shifts as the applied field is rotated away from [110]. The FMR results are analyzed in terms of magnetoelastic anisotropy and compared to LCMO/STO grown under the same conditions. A two-layer magnetization model is proposed, based on strong out-of-plane anisotropy near the BTO interface and shown to qualitatively explain the main characteristics of the FMR results.

DOI: 10.1103/PhysRevB.88.134410 PACS number(s): 77.55.Px, 76.50.+g, 75.30.Gw, 77.80.−e

I. INTRODUCTION

Recently, ferroelectric tunnel junctions emerged as efficient realizations of nanoferronics, i.e., the control of various ferroic orders, e.g., ferromagnetism and ferroelectricity, on the nanoscale.[1] These devices consist of two ferromagnetic (FM) layers separated by a very thin ferroelectric barrier, where the quantum-mechanical tunneling between the magnetic layers depends strongly on the electrical polarization of the ferroelectric spacer. Giant tunnel electroresistance was found in devices based on $BaTiO_3$/Fe heterostructures and $BaTiO_3/La_{0.67}Sr_{0.33}MnO_3$.[2,3] These heterostructures have been proposed for logic components beyond complementary metal-oxide semiconductors, nonvolatile electrically controlled random access memories, or as memristors.[4] New magnetoelectric phenomena have been predicted to occur at ferroelectric/FM interfaces. In particular, exotic spin arrangements ranging over a few unit cells near the interface between an optimally doped manganite and a ferroelectric are expected.[5,6] Therefore, in-depth exploration of the effects leading to the magnetoelectric coupling of the layers involved in these heterostructures is desirable, as they can severely affect device performance in spintronics applications.

Several mechanisms may contribute to the coupling between FM and ferroelectric layers.[6–9] The magnetoelectric effect in two-phase systems may be mediated by strain, and this often forms the basis of the search for multiferroic materials.[8–10] Recently, nanopatterned heterostructures,[11] composites,[12,13] or epitaxial multilayers[14,15] have also been investigated. A particular case of strain-driven magnetoelectric effect occurs in heterostructures combining ferroelectric substrates such as $BaTiO_3$ (BTO) and epitaxial FM thin films ($La_{1-x}Sr_xMnO_3$,[16,17] $La_{1-x}Ca_xMnO_3$,[18] $CoFe_2O_4$, and Fe_3O_4).[19,20] In these systems, changes in the FM layer are mediated by the piezoelectric effect of the substrate via magnetoelastic (ME) coupling.

Here, we concentrate on the strong ME coupling observed in $La_{0.7}Ca_{0.3}MnO_3$ (LCMO) epitaxial ultrathin films (10–15 nm) grown on BTO substrates.[16,21,22] Optimally doped LCMO, which is well known for colossal magnetoresistance, is also characterized by its strong tendency towards electronic phase separation.[23] BTO single crystal is an archetypal ferroelectric material with a simple perovskite structure above $T_c = 393$ K. At lower temperatures, BTO undergoes three further phase transitions: tetragonal (T) down to 279 K ($a = 3.994$ A and $c = 4.036$ Å), orthorhombic (O) down to 183 K (equivalent pseudomonoclinic cell constant, $c_m = 4.018$ Å), and rhombohedral (R) at lower temperatures ($a = 4.004$ Å), remaining ferroelectric in all three lower temperature phases.[24,25]

Previously, characterization with grazing incidence x-ray diffraction showed that LCMO/BTO systems are epitaxial at all temperatures and the epitaxial strain is partially relaxed.[21] The lattice mismatch, $\eta = (a\_a_f)/a_f$ (where a_s and a_f are the substrate and thin film parameters, respectively) between LCMO pseudocubic parameter and BTO parameters in the three ferroelectric phases implies epitaxial strains in the 1–2% range. This is the first ingredient for large magnetic anisotropy in LCMO/BTO systems. The second ingredient comes from the substrate corrugation.[26,27] We extensively studied the

surface topography of BTO substrates and LCMO/BTO systems in Refs. 21,22. In the T phase, a corrugation angle of 0.6° appears between a and c domains at the interface with the thin film. This corrugation remains even in the R phase. In this phase a new corrugation angle of 0.27° and characteristic length of 7.6 μm in our samples appears, originating in domain walls corresponding to the various possible polarization orientations. The typical roughness in BTO substrates is 40 Å, one order of magnitude larger than in the T phase of $SrTiO_3$ (STO) substrates.[28] These results are in good agreement with those found in literature.[29]

Remarkable evidence for strong ME coupling in LCMO/BTO comes from the so-called Matteucci-like magnetic hysteresis loops.[21] The exotic shape of the magnetic loops in the temperature range of 40–140 K and the depressed magnetization (from 3.7 to 1.8 μ_B/Mn at 10 K) were explained in terms of magnetostriction-induced changes of magnetic anisotropy based on the hypothesis of two different spin populations: one with in-plane easy axis and the other with negative magnetostriction and out-of-plane easy axis. Thus, an out-of-plane population was postulated to result from high strains and corrugation near the interface with the substrate. We reported evidence[22] compatible with the existence of an antiferromagnetic (AF) phase interspersed within the FM phase, similar to magnetic phase separation in bulk manganites but at larger length scales. The appearance of the AF phases would be triggered by the O to R phase transition of the substrate. These magnetic properties were consistent with the structural coherence volumes (17–90) × 200 × 200 Å^3, determined by x-ray diffraction, leading to a picture of a magnetic-metallic granular system.

In order to elucidate the complex magnetic anisotropy of LCMO/BTO thin films, we naturally turn to FM resonance (FMR).[30,31] We also used polarized neutron reflectometry (PNR) in order to reveal the depth profile of magnetization and locate the two magnetic moment populations. We find a vertical segregated structure in the thin-film magnetic profile. We observe a remarkable difference in the anisotropy of the LCMO/BTO thin films compared to control samples grown on STO in which low strains and no corrugation are expected. Results from both techniques are combined in a model of two magnetic layers coupled ferromagnetically: one thin layer near the interface with out-of-plane anisotropy and the other with in-plane biaxial anisotropy, typical in LCMO thin films. This model qualitatively explains the characteristics of the FMR spectra, confirming the presence of an out-of-plane spin population highly coupled magnetoelastically to the substrate.

II. EXPERIMENTAL

LCMO epitaxial thin films were grown simultaneously on unpoled, nominally [001] oriented BTO and [100] oriented STO single-crystal substrates using high O_2 pressure (3.4 mbar) dc sputtering at 900 °C. Our BTO substrates ($5 \times 5 \times 1$ mm^3) did not experience a poling process during fabrication and thus, exhibit a and c domains in the T phase. The structure was characterized by x-ray diffraction and reflectometry performed on a Bruker D8 four-circle diffractometer (Cu $K_{\alpha 1}$ radiation) equipped with a LynxEye position sensitive detector. The magnetism of the films was characterized with a vibrating sample magnetometer (VSM) to extract the saturation magnetization. FMR experiments were carried out on a JEOL electron spin resonance spectrometer operating in the X band around 8.9 GHz at 77 K.

Polarized neutron reflectometry was performed at the Asterix reflectometer (Los Alamos Neutron Science Center) to investigate the depth profiles of magnetization on both LCMO/BTO and LCMO/STO. For this purpose, samples ($10 \times 10 \times 1$ mm^3) with nominal 120-Å thickness, as determined by room temperature laboratory x-ray reflectometry, were prepared under the same conditions as reported above. For PNR experiments, samples were cooled in zero field to 120 and 30 K (LCMO/BTO) and 90 K (LCMO/STO), that is, to the same temperature relative to their respective Curie temperatures, T_c. Subsequently, a saturating magnetic field (0.6 or 1.0 T, for LCMO/BTO and LCMO/STO, respectively) was applied in plane, along the [110] easy axis. Both nonspin-flip (NSF) and spin-flip (SF) neutron cross sections were explored near the critical angle. In the absence of measurable SF signals, only NSF (R^{++} and R^{--}) reflectivities[32] were recorded as a function of momentum transfer Q. The implications of no measurable SF signals are relevant in LCMO/BTO systems, where an important fraction of magnetic moments is expected to be out of plane and/or antiferromagnetically ordered. That is, within the sensitivity of the technique, all detected magnetic moment is in plane and aligned with the applied field ($M_{\|}$).

For the FMR studies twin samples of t = 120-Å-thick LCMO were grown on STO [100] and BTO [001] substrates. A thicker, t = 150 Å LCMO/BTO was also studied. After growth, the 1-mm-thick substrates were cut to areas of (2×2 mm^2) with a diamond saw. The samples were fixed with vacuum grease (Dow Corning) to small cylindrical Teflon pieces and finally sealed in quartz electron paramagnetic resonance (EPR) tubes (4-mm outer diameter) under 20-mbar He exchange gas. This arrangement permitted both placing the ampoules directly into liquid nitrogen at 77 K and their rotating around an axis perpendicular to the applied magnetic field. The rotation axis was chosen along either of the various crystallographic axes of the substrate: [001] for field rotating in-plane and [100] or [110] for field rotating away from the film plane along one or the other principal directions. The sample holders allowed 1–2° accuracy for the alignment of the sample axis with respect to the rotation axis, whereas the manual rotation of the ampoules invoked an angular accuracy of 3°. For each orientation, spectra were recorded as a function of rotation angle (φ in plane and θ out of plane) at every 5° over 360°. Each recorded spectrum is a derivative of the magnetic field-dependent microwave absorption. The spectra are analyzed with least-squares fitting of derivative Lorentzian lines to extract the field of resonance, using an admixture of absorptive and dispersive contributions to account for the metallic and dielectric distortion effects of the film and ferroelectric substrate.[29]

III. RESULTS

A. PNR magnetization profiles

Polarized neutron reflectometry is a sensitive tool to reveal the magnetization depth profile of thin films and is extensively used in the determination of magnetic profiles in complex

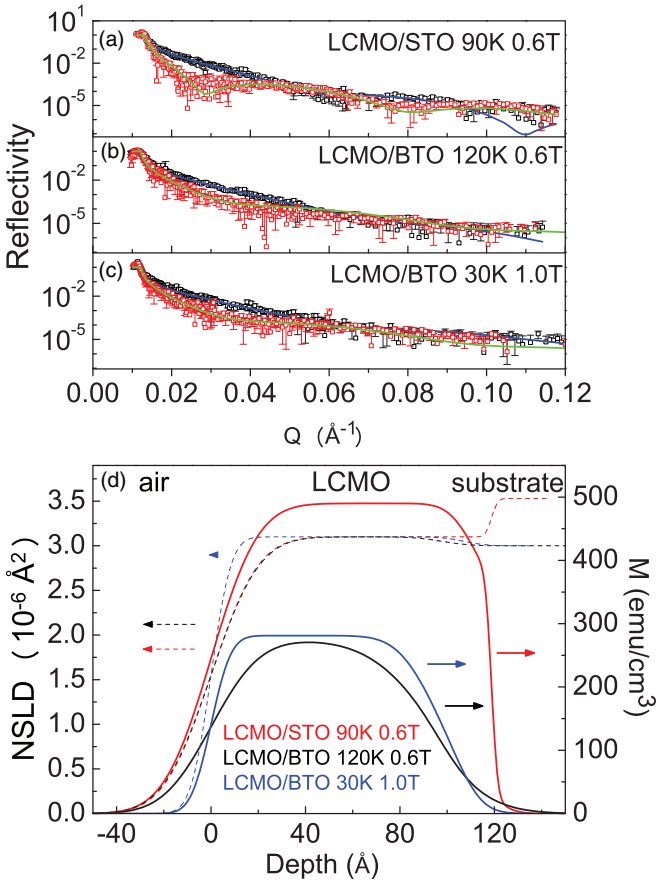

FIG. 1. (Color online) (a)–(c) NSF reflectivities measured on Asterix (Los Alamos Neutron Science Center) and experimental conditions given. (d) Magnetization and NSLD profiles obtained with *co_nevot_croce* from the experimental data. Note the absence of a plateau in the magnetization profile of LCMO/BTO at 120 K, which is present both for LCMO/STO and LCMO/BTO at 30 K.

oxide heterostructures.[33,34] PNR NSF reflectivities were analyzed using the CO-NEVOT-CROCE code, which implements Parrat's formulation to extract nuclear and $M_{\parallel}$ magnetic scattering length profiles.[32] Best fits to experimental data [shown in Fig. 1(a)] were obtained by partitioning the manganite layer profile in two zones: an upper one close to the air interface and a lower one, close to the interface with the substrate. The Nevot-Croce roughness (σ) of the interfaces, thickness (Δ) of the layers, and magnetic scattering lengths (ρ_M) were left as free parameters for the fits. Best values and confidence limits are listed in Table I. The interpretation of profiles for layers with $\sigma \gg \Delta$ is best done in terms of their derivatives with respect to the depth coordinate as discussed in Ref. 35. Figure 1(b) shows the nuclear scattering length density (NSLD) and in-plane magnetization profiles. X-ray reflectivity, having been collected at room temperature in the T phase of BTO, was not included in the PNR data analysis. Given the uncertainty in the density of the LCMO thin layers, during the iterative least-squares fitting process, the NSLD values of the LCMO layers were initially optimized within the $2.5{\cdot}10^{-6}$ to $5.0{\cdot}10^{-6}$ Å^{-2} range. A value of $3.1{\cdot}10^{-6}$ Å^{-2} was consistently obtained as optimal for this parameter and was used for the final LCMO/BTO and LCMO/STO fits. This NSLD value is 15% smaller than the one corresponding to LCMO bulk density, a fact that in LCMO/BTO may be attributed to the relaxed state of the layer and to corrugation of the substrate interface. This latter possibility can be assessed by a simple geometrical model accounting for various proportions of air, LCMO and BTO being probed at constant depth. With the aid of this simple model, for a neutron beam with a coherence length of 1 μm impinging on a flat section of a corrugated interface such as that reported in Ref. 22, an averaged NSLD of $3.1{\cdot}10^{-6}$ Å^{-2} ($3.3{\cdot}10^{-6}$ Å^{-2}) for the layer region is obtained for corrugation angles of 0.9° (0.6°).

The calculation of the total thickness ($\Delta_A + \Delta_B$) from the PNR data, taking into account the optimal values for Δ_A and Δ_B and the estimated unsymmetrical error bars for Δ_A, yields an upper value of (98 + 2) Å = 100 Å at 120 K and a lower value of (107–3) Å = 104 Å at 30 K (see Table I). Additionally, there is uncertainty in Δ_B that has not been quantified due to the strong correlation between Δ and σ parameters but may very well bridge the 4-Å difference in the extreme values given above. Thus, within experimental error, we conclude that total thickness is not changing significantly with temperature.

It is apparent that near the LCMO/BTO interface, no significant differences in NSLD exist between the results on BTO at 120 and 30 K. However, the difference in $M_{\parallel}$ magnetization profiles is significant: the measurements on BTO at 30 K (and on STO) show a significant plateau in the central part of the magnetization profile and a steep decrease when approaching the substrate interface. On BTO at 120 K, this plateau is absent, and $M_{\parallel}$ decreases steadily from its

TABLE I. Fitted values for the two-zone model for the LCMO layer. Numbers in parentheses correspond to 68% confidence limits for the best value shown. An asterisk (*) indicates unrealistic values for the upper and lower confidence limits due to the strong correlation between Δ and σ parameters.

Sample	Air/LCMO interface σ (Å)	LCMO upper zone (A) Δ (Å)	LCMO upper zone (A) σ (Å)	LCMO upper zone (A) ρ_M (10^{-6} Å^{-2})	LCMO bottom zone (B) Δ (Å)	LCMO bottom zone (B) σ (Å)	LCMO bottom zone (B) ρ_M (10^{-6} Å^{-2})
LCMO/STO 90 K 0.6 T	16 (15.8–16.3)	112 (111–113)	9 (8–10.4)	1.4 (1.38–1.44)	7 (5.4–8.7)	2 (0.4–3)	1.0 (0.8–1.4)
LCMO/BTO 120 K 0.6 T	16 (15.5–16.9)	92 (88–94)	21 (12–25)	0.8 (0.74-0.82)	6 (*)	9 (*)	0.1 (0–0.3)
LCMO/BTO 30 K 1.0 T	7 (4.6–7.8)	94 (91–98)	12 (6–23)	0.8 (0.76–0.84)	13 (*)	7 (*)	0.2 (0–0.3)

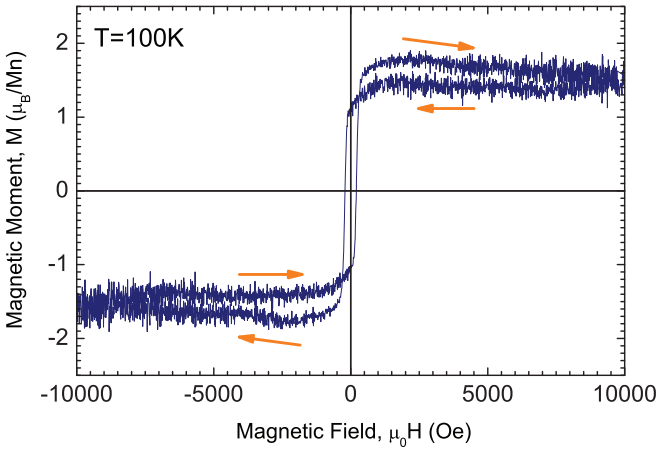

FIG. 2. (Color online) Characteristic magnetic hysteresis loop of a Matteucci LCMO/BTO sample, at 100 K. No FMR was observed for this sample at 8.9 GHz.

maximum value near the center of the LCMO layer to the interface with BTO (note that best-fit parameters for this zone of the LCMO layer imply $\sigma > \Delta$). We interpret this as evidence of a depletion of magnetic moments aligned with the saturating magnetic field on LCMO/BTO at 120 K when compared with the same system at 30 K. From our experiments, however, it is impossible to decide whether this depletion arises from a significant population of out-of-plane magnetic moments or by a vector cancellation of in-plane magnetizations corresponding to magnetic domains whose magnetic coherence length is smaller than the neutron beam coherence length (estimated in the range of 1–10 μm).

B. FMR spectra

FMR spectra were recorded at 77 K for four different thickness samples: three LCMO/BTO thin films, one of t = 150 Å, and two of t = 120 Å—one of the latter exhibiting Matteucci magnetic loops (see Fig. 2) did not yield any observable FMR—and a reference LCMO/STO with t = 120 Å. The diagram in Fig. 3 shows the different orientations of the applied magnetic field, $\mathbf{B}_{\text{applied}}$, with respect to the film surface and the corresponding values of the orientation angles. Figures 4–6 show the FMR spectra for the LCMO/STO, LCMO/BTO (150 Å) and LCMO/BTO (120 Å), respectively. The spectra are offset vertically by the corresponding orientation angle of the applied field. Left panels show the in-plane rotations where 0° denotes field applied along the

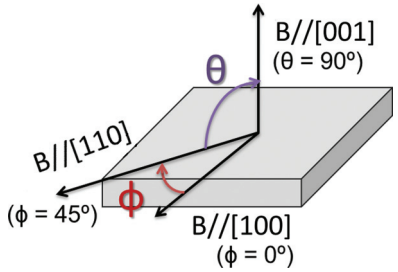

FIG. 3. (Color online) Schematics of the geometry of magnetic field with respect to the LCMO film.

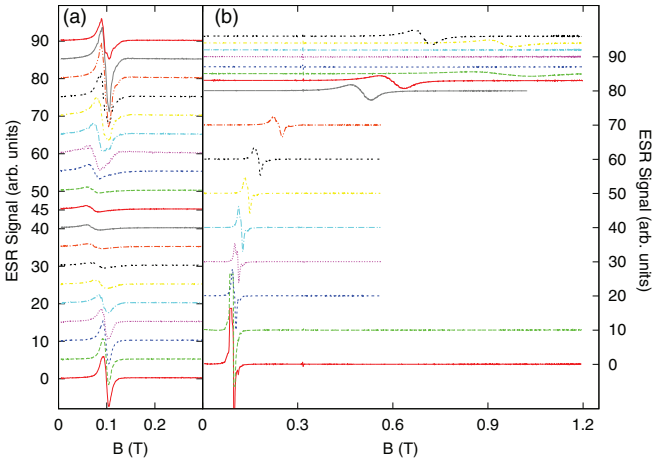

FIG. 4. (Color online) FMR spectra with various magnetic field orientations in plane (a) and out of plane (b) of a 120-Å-thick LCMO film on STO at 77 K. The spectra are offset for clarity, and their baseline value corresponds to the orientation angle (φ in plane and θ out of plane; see Fig. 3).

[100] direction: B//[100] and 45° along the B//[110] direction. Right panels show rotations from B//[100] to the B//[001] (out-of-plane) direction for LCMO/STO and rotations from B//[110] to the B//[001] direction for LCMO/BTO. For all four films, out-of-plane rotations reveal the hard axis, along [001], and in-plane rotations show an in-plane easy axis along [110], where the resonance field, denoted as B_0, is observed. However, several striking differences can be observed:

(1) The FMR signal is much weaker in LCMO/BTO than in LCMO/STO.

(2) LCMO/BTO shows considerably broader resonances and, unlike for LCMO/STO, these get sharper near the B//[110] and B//[001] directions.

(3) For LCMO/BTO when the applied field is rotated away from the film plane, no FMR can be conclusively identified

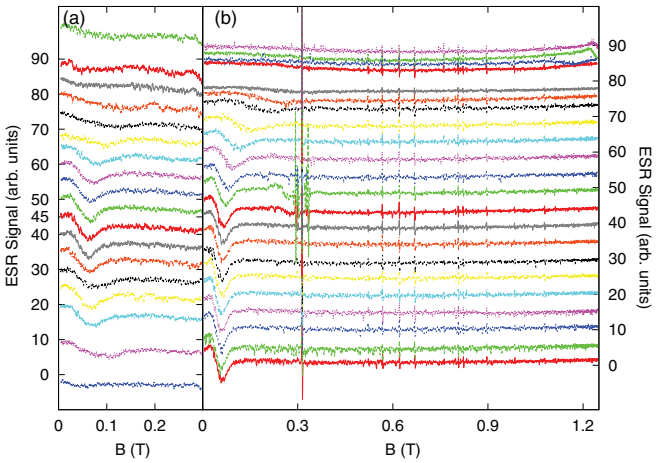

FIG. 5. (Color online) FMR spectra with various magnetic field orientations in plane (a) and out of plane (b) of a 150-Å-thick LCMO film on BTO at 77 K. The spectra are shifted vertically, and their baseline value corresponds to the orientation angle. The resonance around 0.3 T is DPPH used as a reference.

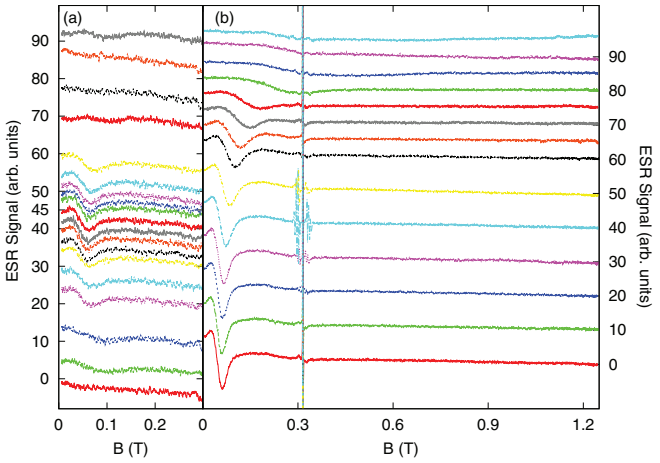

FIG. 6. (Color online) FMR spectra with various magnetic field orientations in plane (a) and out of plane (b) of a 120-Å-thick LCMO film on BTO at 77 K. The spectra are shifted vertically, and their baseline value corresponds to the orientation angle. The resonance around 0.3 T is DPPH used as a reference.

in an experiment where the in-plane direction is along [100] [Figs. 5(a) and 6(a)].

(4) For LCMO/BTO when the field rotation starts from [110] and progresses towards [001], the FMR is well resolved up to approx. $\theta \sim 75$–80°, and the FMR shifts to higher field rather slowly, staying near the easy-axis value.

(5) Close to B//[001] for LCMO/BTO, or perpendicular to the film plane, the FMR appears as a sharp resonance at high field, just below the limit of the maximum field of the spectrometer [Fig. 5(b)].

The obtained resonance fields (B_0) are plotted vs the rotation angle in Figs. 7(a)–7(c) (in-plane rotations) and Figs. 7(d)–7(f) (out-of-plane rotations) for LCMO/STO (120 Å), LCMO/BTO (150 Å), and LCMO/BTO (120 Å), respectively. FMR for both LCMO/BTO [Figs. 7(e) and 7(f)] was measured with B field between [110] in plane ($\theta = 0^\circ$, see Fig. 3) and [001] out of plane ($\theta = 90^\circ$). For LCMO/STO [Fig. 7(d)] the in-plane direction was less critical and was chosen as [100] ($\theta = 0^\circ$). The in-plane data [Figs. 7(a)–7(c)] show typical sinusoidal variation, characteristic of biaxial symmetry with easy axes along the four [110] directions. However, as Figs. 5 and 6 demonstrate, around [100], no resonance could be resolved in LCMO/BTO. In out-of-plane rotations of LCMO/BTO [Figs. 7(e) and 7(f)], the FMR barely shifts until 50° and then starts to slowly creep upwards up to 75° where it rapidly broadens and disappears. Sharper resonances appear around 1 T near the [001] orientation in the thicker LCMO/BTO (150-Å) film. Narrow lines in the spectra around 0.33 T ($g = 2$) correspond to the EPR of the reference 2,2-diphenyl-1-picrylhydrazyl (DPPH). Other angular-dependent lines around 0.6 T correspond to EPR of defects in the substrates.

C. Anisotropy energies

For the interpretation of the FMR results, we use a classical free-energy anisotropy model to determine first the equilibrium magnetization orientation for a given applied field (magnitude and direction): $\mathbf{M}(\mathbf{B}_{\text{applied}})$ and the eigenoscillation around this equilibrium. We then vary the magnitude of $\mathbf{B}_{\text{applied}}$ until the eigenfrequency equals the frequency of the simulated experiment, we denote $\mathbf{B}_{\text{applied}}$ by B_0. The free energy includes the Zeeman energy, shape anisotropy terms, and the power series of the directional cosines as the anisotropy energy:[36]

$$E/V = -\mu_0 \mathbf{M}\cdot\mathbf{B}_{\text{applied}} + 1/2\,\mu_0 \mathbf{M}\cdot\underline{\mathbf{N}}\cdot\mathbf{M} + K_{2c}\alpha_3^2 + K_{4ab}\left(\alpha_1^4+\alpha_2^4\right) + K_{4c}\alpha_3^4, \quad (1)$$

where V is the volume of the FM layer, α_1, α_2, and α_3 are the direction cosines of the LCMO magnetization ($\alpha_i = \mathbf{M}_i/\mathbf{M}_{\text{sat}}, i = 1,2,3$ and $\alpha_1^2+\alpha_2^2+\alpha_3^2 = 1$), $\underline{\mathbf{N}}$ is the demagnetization tensor [$(N_{11},N_{22},N_{33}) = (0,0,1)$ in the case of a film perpendicular to the z axis], K_{2c} is the lowest order out-of-plane anisotropy term, K_{4c} the next order, K_{4ab} is the lowest order in-plane anisotropy term, and M_{sat} is the saturation magnetization (determined using VSM).

For the $t = 120$-Å-thick LCMO/STO layer, we obtained $K_{2c} = (+140 \pm 30\ \text{kJ/m}^3$ and $K_{4ab} = (+1.7 \pm 0.5\ \text{kJ/m}^3$ (see Table II). No higher order terms appearing in Eq. (1) were needed to describe the fundamental features of LCMO/STO. Simulations of the angular dependence of the FMR B_0 with these parameters are shown in Figs. 7(a) and 7(d). In Ref. 37, somewhat lower values, $K_{2c} = (+48\ \text{kJ/m}^3$ and $K_{4ab} = (+1.6\ \text{kJ/m}^3$, were obtained for a $t = 150$-Å-thick LCMO/STO.

FMR spectra of a $t = 120$-Å LCMO/BTO, not exhibiting Matteucci loops, are shown in Fig. 6. As in the case of the 150-Å-thick LCMO/BTO, no resonance was observed near the B//[100], and although B//[110] remains the easy axis, its shift to higher fields is small [Fig. 6(a)] away from [110]. The out-of-plane rotations are in Fig. 6(b); again, resonance fields shift slowly up when rotating to B//[001], remaining at $B_0 \sim 0.3$ T even at 80°. In the thinner layer, no resonance was observed around B//[001] within the limit of our spectrometer. Compared with LCMO/STO, broad and weak signals are characteristic of these spectra. Figures 7(c) and 7(f) show the in-plane and out-of-plane angular dependence of the resonance fields, respectively. The corresponding parameters for Eq. (1) of the FMR simulation are summarized in Table II. Remarkably, in another thin 120-Å LCMO/BTO film, which did exhibit Matteucci magnetic loops, no FMR could be observed for any magnetic field orientation.

A strong tendency for out-of-plane orientation of the magnetic moments is apparent in LCMO/BTO: the FMR can be described by incorporating the fourth-order out-of-plane K_{4c} term, with values given in Table II. The salient feature of these results is the large and negative $K_{4c} = (-70 \pm 20\ \text{kJ/m}^3$ for the thicker $t = 150$-Å LCMO/BTO and even larger $K_{4c} = (-140 \pm 20\ \text{kJ/m}^3$ for the $t = 120$-Å thinner film. Indeed, the out-of-plane FMR of LCMO/BTO cannot be described without recurring to the K_{4c} term, not needed for LCMO/STO. This large, negative, K_{4c} term yields the low values of the resonance field near [001]. Indeed, the curious backwards turn of the simulation near [001], indicated with an arrow in Fig. 7(f) is a direct consequence of K_{4c} being comparable to K_{2c} but negative.

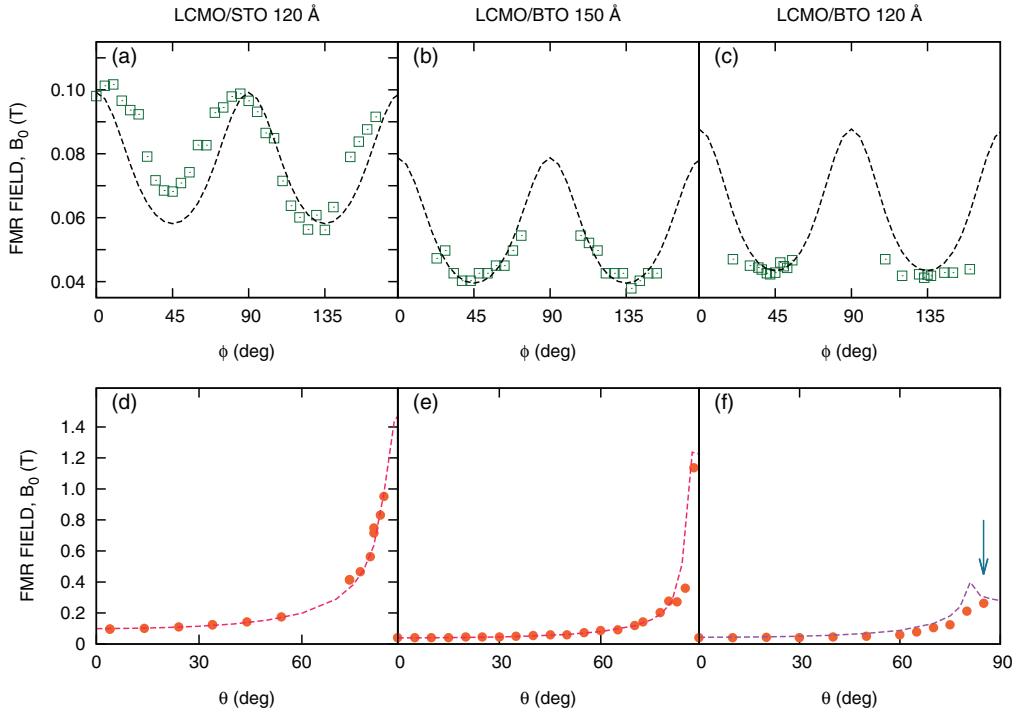

FIG. 7. (Color online) FMR fields for LCMO/STO 120 Å in plane (a) and out of plane (d), LCMO/BTO 150 Å in plane (b) and out of plane (e), and LCMO/BTO 120 Å in plane (c) and out of plane (f), as extracted from FMR spectra shown in Figs. 4–6. Lines correspond to simulations using Eq. (1) and parameters listed in Table II.

The large, negative K_{4c} indicates the existence of a fraction of magnetic moments that prefer to be out of plane in LCMO/BTO. The overall energy balance, K_{2c}, and the shape anisotropy, keep the film plane as the easy plane of the system. Yet, a negative K_{4c} comparable to K_{2c} is needed to simulate the low resonance field, implying a tendency of spins to be out of plane. The nonuniform distribution of magnetization extracted from PNR depth profiles indicates that the nonaligned population of spins must reside near the interface with the substrate. The influence of these out-of-plane spins in the macroscopic properties is thickness dependent. In thicker layers ($t > 150$ Å), the effect of these spins in magnetic, and transport properties weakens.[22] In this sense, the relative amount of the two populations plays an important role. We consider the ratio t^B/t^A, where t^B is the thickness of the sublayer at the interface with BTO estimated from PNR (see Fig. 1) to be 30 Å and t^A is the thickness of the more relaxed sublayer further from the BTO. As t^A increases with LCMO film thickness, K_{4c} diminishes (Table II). Also, the small reduction of K_{2c} in the thinner layer can be a result of an increase of K_{4c}. In this respect, LCMO/STO can be considered as the limit $t^B \to 0$.

IV. DISCUSSION

The most surprising results of the PNR and FMR experiments are the depressed magnetization near the interface and the large negative K_{4c} anisotropy constant. We discuss our results of the anisotropy energies first in terms of the ME energy density by developing the relevant anisotropy terms to second order in strains. We will see how second-order effects predict large negative K_{4c} coefficients but then also bring about large variations in K_{4ab} terms. We then use the PNR observation of depressed magnetization near the LCMO/BTO interface and introduce a two-layer magnetic model. We construct this model, motivated by the Matteucci loops, of a thin interfacial layer of strong out-of-plane oriented moments and a thicker layer with magnetic properties similar to LCMO/STO, coupled ferromagnetically. We will restrict as many of the model parameters based on other experiments (PNR, magnetometry, FMR of LCMO/STO) as possible. The phenomenological properties of the two-layer model are then discussed in terms of the effects of the remaining parameters, and we compare the predictions of the simulations to the observed FMR of LCMO/BTO. What guides us in selecting

TABLE II. Anisotropy energies of $t = 120$ Å LCMO/STO and LCMO/BTO and $t = 150$ Å LCMO/BTO at 77K. t^B is the estimated 30-Å thickness of the highly strained sublayer near the BTO.

	K_{2c} [kJ/m^3]	K_{4c} [kJ/m^3]	K_{4ab} [kJ/m^3]	M_{sat} [kA/m]/m_{sat}[μ_B/Mn]	t^B/t^A
LCMO/STO (120 Å)	140 ± 30	—	1.7 ± 0.5	400/2.52	0
LCMO/BTO (150 Å)	220 ± 30	$(-70 \pm 20$	2.1 ± 0.7	379/2.38	0.25
LCMO/BTO (120 Å)	190 ± 50	$(-140 \pm 20$	2.1 ± 0.7	375/2.36	0.33

the model-parameter values is the list of salient features of the FMR spectra of LCMO/BTO (Sec. III B). This will force us to use large out-of-plane and biaxial in-plane anisotropies, as expected from the second-order ME effects.

A. ME energy density

Internal strains in thin films due to the substrate (as high as 2% in LCMO/BTO[21]) significantly affect the magnetic anisotropy through ME coupling. This is usually described phenomenologically as an expansion of free energy density in powers of strains, ε_{ij}:

$$E/V = K_{ij}\alpha_i\alpha_j + B_{ij}\alpha_i\alpha_j\varepsilon_{ij} + D_{ijkl}\alpha_i\alpha_j\alpha_k\alpha_l\varepsilon_{ij}\varepsilon_{kl} + \cdots + C_{ijkl}\varepsilon_{ij}\varepsilon_{kl} + \cdots \quad (2)$$

This expansion includes the magnetocrystalline anisotropy (MCA) energy density, with coefficients K_{ij} as the zero-order term, the ME energy density with coefficients of first (B_{ij}) and second (D_{ijkl}) order, as well as the elastic energy density terms (C_{ijkl}).[36,38–40] When strains are less than 1%, as in the case of LCMO/STO, only linear terms are needed. Then, by minimizing the elastic and ME contributions and incorporating them to the MCA, it is possible to calculate analytical expressions for the anisotropy constants of Eq. (1). For a cubic system, assuming a coherently strained film with in-plane strain $\varepsilon_{xx} = \varepsilon_{yy} = \varepsilon$, ignoring shear in plane, $\varepsilon_{xy} = 0$, and denoting the out-of-plane strain as $\varepsilon_{zz} = \varepsilon_z$, the anisotropy constants in Eq. (1) can be expressed as follows:

$$\begin{aligned} K_{2c} &= K_{2z,\mathrm{MCA}} + B_1(\varepsilon_z - \varepsilon) + B_2^2/(2c_{44}) \\ K_{4ab} &= K_{4xy,\mathrm{MCA}} \\ K_{4c} &= \mathrm{K}_{4z,\mathrm{MCA}} + B_2^2/(2c_{44}), \end{aligned} \quad (3)$$

where B_1 and B_2 are the ME coefficients, c_{44} the elastic modulus and $K_{2z,\mathrm{MCA}}$, $K_{4xy,\mathrm{MCA}}$, and $K_{4z,\mathrm{MCA}}$ are the MCA coefficients.[41–43]

For higher strains (1–3%) and in the presence of corrugation at the interface, terms quadratic in strains are needed.[22,27,38,40,44–46] High corrugation can cause larger shears that, in turn, strongly affect the anisotropy, yielding very complex analytical expressions, beyond the scope of this work. Nonetheless, assuming cubic symmetry, with zero in-plane shear, $\varepsilon_{xy} = 0$, but small out-of-plane shears, ε_{xz} and ε_{yz}, (i.e., terms of the form $\varepsilon_{ij}\ \varepsilon_{\ kl}$ and $\varepsilon_{ii}\ \varepsilon_{\ kl}$ are neglected) similar calculations can lead to expressions for the anisotropy constants. Thus, the proposed approximations eliminate a considerable number of ME coefficients and the anisotropy constants read as

$$\begin{aligned} K_{2c} &= K_{2z,\mathrm{MCA}} + B_1(\varepsilon_z - \varepsilon) + B_2^2/(2c_{44}) \\ K_{4ab} &= K_{4xy,\mathrm{MCA}} + D_{12}\,\varepsilon\,\varepsilon_z + D_{11}\,\varepsilon^2 \\ K_{4c} &= K_{4z,\mathrm{MCA}} + B_2^2/2\mathrm{c}_{44} + D_{12}\,\varepsilon^2 + D_{11}\,\varepsilon_z^2, \end{aligned} \quad (4)$$

where the dependence of K_{4c} and K_{4ab} on strains is now explicit. When strains are small, K_{4c} is dominated by $K_{4z,\mathrm{MCA}}$. Since B_2 is proportional to magnetostriction, λ_{111}, B_2^2 is considerably smaller than B_1 and the term $B_2^2/(2c_{44})$ can be neglected.[46] This results in the expected $K_{2c} \neq 0$ and $K_{4c} \approx 0$ for systems like LCMO/STO. Now, the case of high strains includes new ME coefficients (D_{12} and D_{11} in this approximation) that add to the anisotropy constants. Thus, negative ME coefficients can lead to the high negative value of K_{4c} coefficient in LCMO/BTO thin films.

B. The two-layer model

The idea of two different populations of spins in LCMO/BTO, as postulated in Ref. 21, comes naturally from the PNR and FMR results. One population corresponds to relaxed LCMO, akin to LCMO/STO, with in-plane magnetic anisotropy (positive K_{2c}). The other one is highly affected by inhomogeneous strain from the BTO substrate, with out-of-plane anisotropy (negative K_{2c}). By considering these two regions, the magnetic granularity and many of the unusual properties observed in magnetism and transport can be explained.[21]

It is the large out-of-plane anisotropy (indicated by the negative K_{4c}) determined by FMR and the strongly suppressed depth-dependent in-plane magnetization, seen by PNR, that lead us to postulate a two-layer model here. In the following, we discuss the model, and simulations of the corresponding angle-dependent FMR. We express the free-energy areal density of the system as the sum of two different populations of spins distributed as layers of different thicknesses, coupled at the interface:

Sublayer A: We assume a top layer with anisotropy constants found for LCMO/STO with in-plane easy axis: $K_{2c}^{\mathrm{A}} = +140$ kJ/m^3 and $K_{4ab}^{\mathrm{A}} = +1.7$ kJ/m^3 (see Table II) and saturation magnetization, based on VSM measurements: $\mathbf{M}_{\mathrm{A}} = 379$ kA/m (2.5 μ_{B}/Mn).

Sublayer B: For the bottom layer, highly affected by the BTO substrate, we assume out-of-plane easy axis, i.e., negative anisotropy constant $K^{\mathrm{B}}{}_{2c}$. Here, we proceed as suggested in Ref. 44, where the negative K_{4c} is included as an effective K_{2c} that accounts for the large strains and corrugation. In addition, according to Eq. (4) a large, negative, $K^{\mathrm{B}}{}_{4ab}$ can be expected. The thickness and magnetization of this sublayer are estimated from PNR as $t^{\mathrm{B}} = 30$ Å and $\mathrm{M}^{\mathrm{B}} = 50$ kA/m (0.3 μ_{B}/Mn).

We consider in the free energy the corresponding volumetric Zeeman and shape anisotropy terms and finally the simplest coupling between sublayers, an interfacial exchange type FM coupling of the adjacent Mn ions. The resulting free-energy density is

$$\begin{aligned} E/A = &\left[-\mu_0\mathbf{M^A}\cdot\mathbf{B}_{\mathrm{applied}} + {}^1\!/_2\,\mu_0\mathbf{M^A}\cdot\underline{\mathbf{N}}\cdot\mathbf{M^A}\right. \\ &\left. + K_{2c}^{\mathrm{A}}{\alpha^{\mathrm{A}}}_3{}^2 + K_{4ab}^{\mathrm{A}}\left({\alpha^{\mathrm{A}}}_1{}^4 + {\alpha^{\mathrm{A}}}_2{}^4\right)\right]\cdot t^{\mathrm{A}} \\ &+\left[-\mu_0\mathbf{M^B}\cdot\mathbf{B}_{\mathrm{applied}} + {}^1\!/_2\,\mu_0\mathbf{M^B}\cdot\underline{\mathbf{N}}\cdot\mathbf{M^B} + K_{2c}^{\mathrm{B}}\,{\alpha^{\mathrm{B}}}_3{}^2\right. \\ &\left. + K_{4ab}^{\mathrm{B}}\left({\alpha^{\mathrm{B}}}_1{}^4 + {\alpha^{\mathrm{B}}}_2{}^4\right)\right]\cdot t^{\mathrm{B}} - J_{\mathrm{eff}}\,\rho_S\,\mathbf{S}^{\mathrm{A}}\,\mathbf{S}^{\mathrm{B}}, \end{aligned} \quad (5)$$

where ${\alpha^j}_{\mathrm{i}} = \mathbf{M}^j{}_{\mathrm{i}}/\mathrm{M}^j{}_{\mathrm{sat}}$, $i = 1,2,3$ and ${\alpha^j}_1{}^2 + {\alpha^j}_2{}^2 + {\alpha^j}_3{}^2 = 1$, $j =$ A or B is the sublayer index, $\underline{\mathbf{N}}$ is the demagnetization tensor [$(\mathrm{N}_{11},\mathrm{N}_{22},\mathrm{N}_{33}) = (0,0,1)$, A is the (arbitrary) surface area of the layer, ρ_S is the surface density of Mn ions (spins/area), $S^j = M^j/((-g^j \times \mu_{\mathrm{B}} \times \rho^j)$ is the polarization (expectation value) of the spin in the jth layer, ρ^j is the density of the spins in the jth layer, $g^j = 2$ is the gyromagnetic factor, and $t = t^{\mathrm{A}} + t^{\mathrm{B}}$ is the total LCMO film thickness. We focus on simulations (maps of FMR intensity over the magnetic field/excitation frequency plane) for the $t = 150$-Å-thick LCMO/BTO film. With the experimental values of M^{A}, M^{B},

TABLE III. Simulation parameters at 77 K used in the two-layer modes described by Eq. (5). The coupling value used is $J_{\text{eff}} \approx 4{\cdot}10^{-23}$ kJ $\sim$ 250 meV per spin pair.

	K_{2c} [kJ/m^3]	K_{4ab} [kJ/m^3]	M_{sat}[kA/m]	t [Å]
Sublayer A	140	1.7	379	120
Sublayer B	$(-220 \pm 30$	$(-50 \pm 10$	50	30

t^{A}, and t^{B}, and the anisotropy constants of the LCMO/STO layer, only $K^{\text{B}}{}_{2c}$, $K^{\text{B}}{}_{4ab}$, and J_{eff} remain as free parameters for the simulations. We selected these to capture most of the qualitative features of the experimental FMR listed in Sec. III B. Table III gives the values best approximating the experimental results, as described below.

The resonance modes and frequencies of this system of coupled FM layers can be calculated once all the parameters, including the size and direction of $\mathbf{B}_{\text{applied}}$ are fixed: We determine first the equilibrium orientation of $\mathbf{M}^{\text{A}}$ and $\mathbf{M}^{\text{B}}$ by minimizing E. Then the coupled equations of motion for $d\mathbf{M}^j/dt^j = \gamma^j (\mathbf{M}^j \times \mathbf{B}_{\text{eff},}{}^j)$ are solved after linearization for small variations of $\mathbf{M}^j$ from their equilibrium. The coupling emerges from the (dynamic) exchange torque produced by the layers on each other. To simulate the orientation dependence of the FMR (recorded by sweeping $\mathbf{B}_{\text{applied}}$ at a fixed frequency), for each orientation, we varied the magnitude of $\mathbf{B}_{\text{applied}}$ systematically until one of the resonance frequencies matched the measurement frequency of 8.9 GHz.

The FMR mode can exhibit fairly complex behavior, especially for the two-layer model. For comparison, simulations for LCMO/STO are shown in Figs. 8(a)–8(c). These 2D FMR maps show expected microwave absorption (in a false color scale) as a function of the excitation frequency and applied magnetic field, at three representative orientations: with the magnetic field applied along the two principal in-plane directions [100] and [110] and in the out-of-plane orientation [001]. The shift of the whole mode between the in-plane easy and hard axes is determined by K_{4ab}. Around the hard axis, the resonance mode is dominated by K_{2c}, where Zeeman and anisotropy energies compete in the magnetization process, resulting in the initial downturn of the resonance mode and its final upturn [Fig. 8(c)] for strong enough fields to reach magnetic saturation [Fig. 8(i), black line, around 1.2 T]. The FMR mode crosses the excitation microwave frequency (indicated as green lines at 8.9 GHz) at smaller magnetic field in the expected [110] direction, in agreement with this being the easy axis given by the positive K_{4ab} of the simulation. In the out-of-plane orientation [Fig. 8(c)] the resonance is predicted above the experimentally available magnetic field (at $\mathbf{B} = 1.2$ T), in accordance with no resonance observed for this direction in Fig. 4. The relative intensity of the resonances at different orientations observed in LCMO/STO spectra is also reproduced: the intensity of the resonance near the easy axis is lower than around B//[100].

We employ the two-layer model of Eq. (5) to describe the magnetism of LCMO/BTO. A complex FMR mode results from the coupling of the individual resonances of the two sublayers. The model has nine parameters of which we fix six based on experiment, as discussed above: the two magnetizations, the sublayer thicknesses, and the in-plane

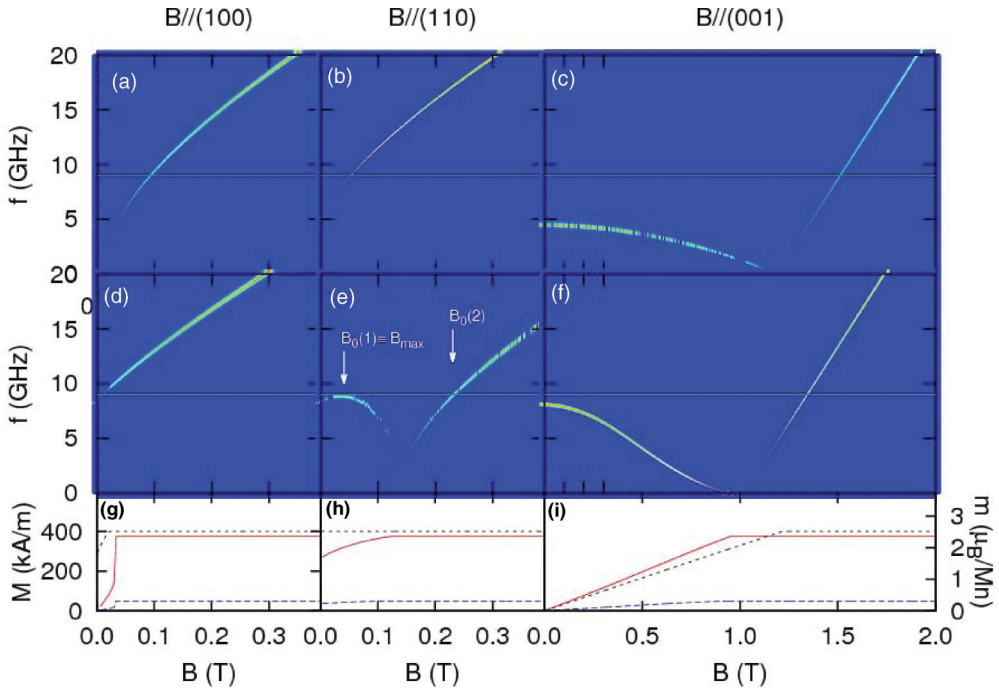

FIG. 8. (Color online) FMR maps calculated for the LCMO/STO 120-Å layer [upper panels (a)–(c)] and the LCMO/BTO 150-Å layer [central panels (d)–(f)] in three selected applied field orientations B//[100], B//[110], and B//[001]. For the LCMO/STO layer, a one-layer model described by Eq. (1) was used. For LCMO/BTO, the two-layer model described by Eq. (5) was used. Green lines indicate the experimental microwave excitation frequency of 8.9 GHz. Lower panels [(g)–(i)] show the simulated magnetization in the direction of the applied magnetic field for LCMO/STO (black), and LCMO/BTO top sublayer A (red), and bottom sublayer B (blue).

$K^{A}{}_{4ab}$ and out-of-plane $K^{A}{}_{2c}$ anisotropy constants of the top layer. There is no obvious guidance from experiment for the other three parameters: $K^{B}{}_{4ab}$, $K^{B}{}_{2c}$, and the A-B layer coupling, J_{eff}. We studied a large set of simulated FMR maps varying all three parameters systematically, until a parameter set was found that reproduces the important features, described in Sec. III B, of the FMR data qualitatively. These parameters are given in Table III, and the corresponding FMR maps in the three main orientations of the magnetic B field are shown in Figs. 8(d)–8(f). In the following, we discuss each of the free parameters of the two-layer model separately by comparing their effects on the simulated FMR maps to the experiment.

The most striking difference of the FMR maps of the two-layer model with respect to the one-layer model is that in the [110] orientation the low frequency, experimentally achievable, mode shows a maximum frequency in low applied B field, indicated as B_{max} in Fig. 8(e). We tuned this "bump" with the chosen model parameters to be just above the measurement frequency, 8.9 GHz, indicated with a green line. In-plane characteristics of the observed spectra in LCMO/BTO are determined mainly by $K^{B}{}_{4ab}$. The model forces us to use a large negative $K^{B}{}_{4ab}$ anisotropy constant in order to push the B_{max} bump up to observable frequencies. For certain orientations near [110] of the applied B field, the two-layer model predicts more than one FMR peaks. We identify the experimental FMR with the low-field peak, $B_0(1) \sim B_{max}$ and will comment below on why the higher-field peak, $B_0(2)$ reminiscent of the resonance of the one-layer model, is not observed except for near perpendicular directions. Figures 8(d)–8(f), show the FMR maps with $K^{B}{}_{2c} = (-220\ \text{kJ/m}^3$, $K^{B}{}_{4ab} = (-50\ \text{kJ/m}^3$, and $J_{\text{eff}} = 4{\cdot}10^{-23}$ kJ (∼250 meV) per interfacial spin pair to simulate the observed FMR of 150-Å-thick LCMO/BTO.

When the magnetic field is applied near [110], the direction where FMRs were experimentally observed, the two-layer model gives FMR modes with a minimum frequency (at fields above B_{max} of the bump), corresponding to the reorientation/saturation of the magnetization. In low fields, the bottom layer magnetization forces the top layer magnetization to bend towards [100] and [001]. This minimum frequency slowly rises and then disappears as the field is oriented towards [100], as shown in Fig. 9. Crucially, at the experimental 8.9-GHz frequency, the observed FMR is more intense near [110] than along B//[100], and it is also broadened around B//[110]. Both effects are direct consequences of the bump feature of the resonance around 0.04 T, since the observation at fixed frequency cuts the mode tangentially, precisely near [110]. This $B_0(1)$ resonance in Fig. 9 barely moves when rotating in plane and finally disappears towards B//[100], concurrent with the lack of resonance observed there in LCMO/BTO. Quantitatively, the simulated FMR disappears already 10° away from [110] contrary to experiment, where it is observed up to 20° away, indicating the limits of our model. Nevertheless, the model predicts $B_0(1)$ to be smallest at B//[110], in agreement with experiment.

Figure 10 shows FMR maps using the same model parameters but different top-layer thickness. Interestingly, for a total layer of 120 Å, the resonance mode is raised over the experimental frequency, coinciding with the lack of observable resonance in the LCMO/BTO Matteucci sample. At

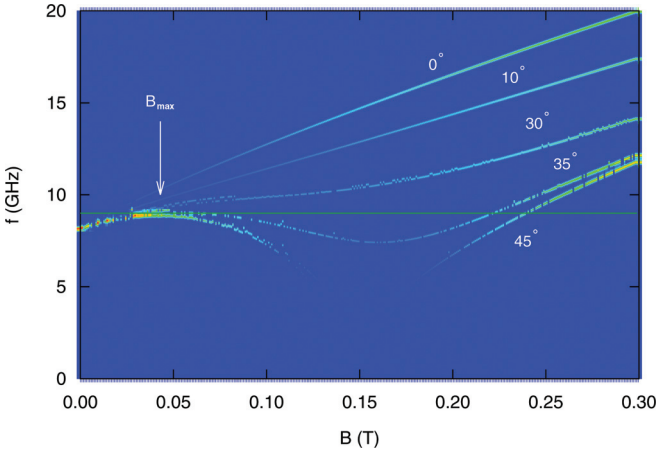

FIG. 9. (Color online) Overlayed FMR maps where B is rotated in plane from B//[100] ($\varphi = 0°$) to B//[110] ($\varphi = 45°$). Resonance $B_0(1)$ ($\sim B_{max}$) is only observed after a certain angle is reached ($\varphi = 35°$ in the model), then it moves to lower fields.

the other extreme, the thickness needed to get the FMR maps to approximate LCMO/STO is 1000 Å with the parameters of Table III. This thickness is much larger than the 250 Å expected experimentally, according to magnetic characterization in Ref. 22. Quantitative agreement between model and experiment is not expected, as the complexity derived from the interface with the inhomogeneous BTO substrate, with varying topography and ferroelectric domain distribution, is addressed in our model only through $K^{B}{}_{4ab}$. As a result, we are forced to use a rather large in-plane $K^{B}{}_{4ab}$ to reproduce the qualitative features of the FMR experiment. Yet, the ME calculations [Eq. (4)] also predict a gain of $K^{B}{}_{4ab}$ with increased strain.

For out-of-plane rotations, it is the corresponding $K^{B}{}_{2c}$ parameter that drives the aspect of FMR. The relative intensity of the resonances in different orientations plays an important role. Near the perpendicular directions a second resonance, denoted as $B_0(2)$, also appears. Figure 11 shows the simulated spectra (extracted from maps, such as Fig. 8) when rotating the field from B//[110] to B//[001]. Initially, the resonance at $B_0(1)$ is more intense and shifts to higher fields rather slowly as it broadens, exactly as observed [Figs. 5(b) and 6(b)]. This is the result of the bump of Fig. 8(e), moving slowly and broadening, when rotating towards the hard axis. In the same process, the sharp and less intense $B_0(2)$ resonance slowly gains intensity and can be finally observed near the hard axis. The observation of this resonance (at low enough fields for the spectrometer) is the natural result of the large and negative $K^{B}{}_{2c}$. The explanation for the process in which the observed lower field resonance [equivalent to $B_0(1)$] loses, and the higher field resonance [i.e., $B_0(2)$] gains, intensity towards the out-of-plane orientation is as follows. The two branches are separated by the field of reorientation/saturation of the magnetization from in plane to out of plane as indicated in Figs. 8(f)–8(i). In strong in-plane fields, the Zeeman energy, the shape anisotropy, and the positive $K^{A}{}_{2c}$ of the top layer, through the FM coupling J_{eff}, all force the bottom layer (B) magnetization to be oriented in plane, along its own hard axis, where it is very sensitive to heterogeneity, given by the highly inhomogeneous BTO

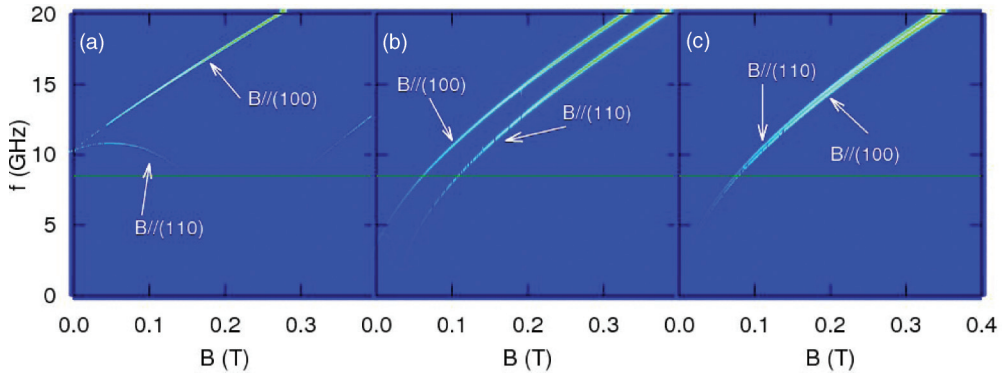

FIG. 10. (Color online) Overlayed FMR maps at two different orientations B//[100] and B//[110] of the two-layer model for three different model thickness: a) 120 Å, b) 500 Å, and c) 1000 Å. Green horizontal line indicates 8.9 GHz.

substrate. This results in strong inhomogeneous broadening of the resonance at $B_0(2)$ (not captured by our model) and its amplitude diminishes rapidly. As the B field is oriented out of plane, it inclines the top layer magnetization away from the plane, causing the coupled $B_0(1)$ resonance frequency to drop below 8.9 GHz and become unobservable, while the resonance at $B_0(2)$ becomes predominant as the bottom layer magnetization approaches its own easy axis, less sensitive to substrate-induced heterogeneity.

The strength of the FM coupling (J_{eff}) determines the shape of the new FMR modes, through the field where the [001] and [110] mode frequencies tend to zero. Decreasing J_{eff} pushes B_{max} to higher frequencies and also increases modestly the resonance field in the [001] orientation [$B_0(2)$]. The actual value of magnetic exchange coupling between Mn spins is hard to determine both experimentally and theoretically.[23,47–49] Nevertheless, it is widely accepted that the effective hopping amplitude between Mn ions (t) must be fractions of an electron volt (from 0.2 to 1 eV) and the on-site Hubbard repulsion (U) to be ∼6 eV.[23] With this, approximating $J_{\text{eff}} \sim t^2/U$, the coupling is expected to be between 5 and 200 meV. In our model, a relatively broad range of values of the FM coupling could reproduce the observations, anywhere between 30 and 300 meV per spin pair, with the appropriate choice of the anisotropy constants and the M^B magnetization. Smaller J_{eff} is needed with stronger M^B, as only their product appears in Eq. (5). Operationally, our choice of the low value of M^B based on PNR leads to the large coupling. In this sense, our J_{eff} must be considered as an effective coupling that accounts for the presence of the much larger out-of-plane moments, not actually included in our model. Physically, even near the interface, there are magnetic moments (M^B, seen by PNR) that can be reoriented in plane with a reasonable applied field. These have a preferred orientation out of plane, due to their coupling to moments, with much larger overall local magnetization that cannot be reoriented easily.

Although our model does not capture the Matteucci physics (magnetostriction was not included), it does provide some insight: the hysteretic behavior between 0.1 and 1 T in

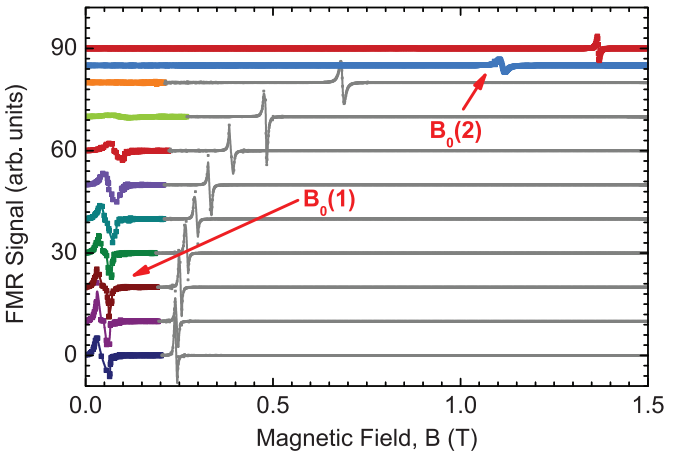

FIG. 11. (Color online) Simulated FMR spectra of the two-layer model with parameters of Table III for t = 150-Å LCMO/BTO in out-of-plane field rotation between B//[110] ($\theta = 0°$) and B//[001] ($\theta = 90°$).

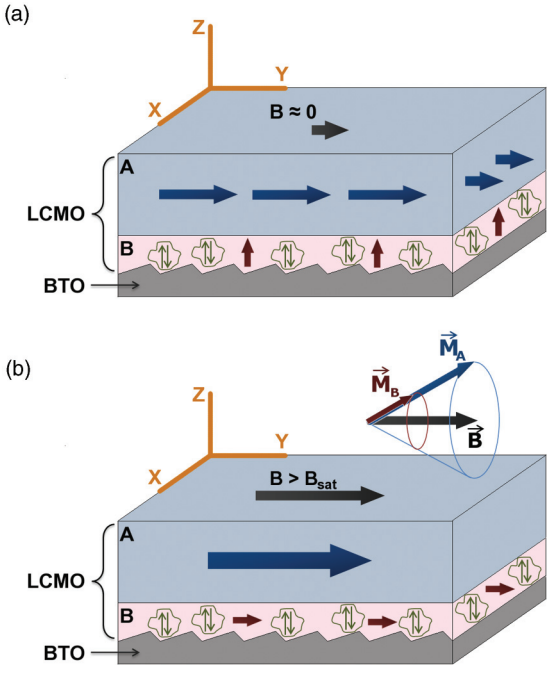

FIG. 12. (Color online) Illustration of the two-layer model. With no applied field, the magnetization near the substrate is out of plane due to out-of-plane anisotropy possibly induced by coupling to AF clusters (a). Under saturating fields M^B turns in plane (b).

Matteucci magnetic loops may have its origin in the magnetic interface between strained and relaxed LCMO. During the magnetization process with increasing applied field in plane, LCMO magnetization at the magnetic grain boundaries rotates out of plane. The actual ferroelectric domain configuration is dramatically different among unpoled BTO substrates.[22] We postulate this as the main reason for the big differences observed between thin LCMO/BTO films. The AF clusters resulting from high strains and corrugation, as discussed in Ref. 22 are not uniformly distributed at the BTO interface. Both FM and AF phases must be interspersed within the bottom layer B, near the interface. Besides, some of these clusters may protrude far into the LCMO, as seen in PNR profiles with overall strongly reduced magnetization. Even in layers as thin as 120 Å, the relative amount of FM and AF populations may vary, as the BTO domain distribution does. We explain this way our observation that some, nominally identical, samples showing Matteucci magnetic loops, have unobservable FMR. This picture of two distinct FM populations with interspersed AF regions is illustrated in Fig. 12. In low applied fields, $\mathbf{M}^{A}$ lays in plane, while $\mathbf{M}^{B}$ keeps out of plane due to the out of plane anisotropy induced by coupling to the AF populations.

V. CONCLUSIONS

We studied the strong ME coupling present in LCMO/BTO by means of the joint analysis of PNR and FMR data. We developed a two-layer magnetic model that satisfactorily addresses the relevant differences of LCMO/BTO FMR spectra compared to LCMO/STO: (i) weak and broadened signals; (ii) absence of resonance around B//[100]; (iii) generally low field resonances $B_0(2)$ near the hard axis; (iv) slow shift of FMR to higher field in out-of-plane rotations; and (v) lack of resonance for Matteucci-like samples. Relying on high strains and corrugation near the interface with the BTO, together with the experimental results from PNR depth profiles, and considering a population of spins near the BTO interface with high negative anisotropy, a relaxed top layer similar to LCMO/STO and a FM coupling between the two FM sublayers, the FMR data are qualitatively explained. Our findings are compatible with the existence of AF clusters resulting from the inhomogeneous strain map and corrugation at the LCMO/BTO interface, with the FM and AF phases interspersed near the interface. Besides, some of these AF clusters may protrude far into the LCMO, as seen in PNR profiles with overall strongly reduced magnetization. Even in layers as thin as 120 Å, the relative amount of FM and AF populations may vary with the BTO domain distribution.

ACKNOWLEDGMENTS

We thank María José Calderón for useful discussions. We acknowledge funding from the Spanish Ministry for Science and Innovation through Grants No. MAT2011-27470-C02-01, No. MAT2011-27470-C02-02, and No. CSD2009-00013. Work supported by the European Research Council Starting Grant No. ERC-259374-Sylo and by the Office of Basic Energy Science (BES), U.S. Department of Energy (DOE), BES-Department of Materials Science funded by the DOE's Office of BES, Division of Materials Research under Grant No. DE FG03-87ER-45332 and Hungarian OTKA Grants K107228 and CNK80991. Los Alamos National Laboratory is operated by Los Alamos National Security LLC under DOE Contract No. DE-AC52-06NA25396.

[1] M. Bibes, Nat. Mater. **11**, 354 (2012).
[2] A. Chanthbouala, V. Garcia, R. O. Cherifi, K. Bouzehouane, S. Fusil, X. Moya, S. Xavier, H. Yamada, C. Deranlot, N. D. Mathur, M. Bibes, Agnès Barthélémy, and J. Grollier, Nat. Mater. **11**, 860 (2012).
[3] L. Bocher, A. e Gloter, A. Crassous, V. Garcia, K. March, A. Zobelli, S. Valencia, S. Enouz-Vedrenne, X. Moya, N. D. Marthur, C. Deranlot, S. Fusil, K. Bouzehouane, M. Bibes, A. Barthélémy, C. Colliex, and O. Stéphan, Nano Lett. **12**, 376 (2012).
[4] J. J. Yang, D. B. Strukov, and D. R. Stewart, Nat. Nanotechnol. **8**, 13 (2013).
[5] S. Dong, X. Zhang, R. Yu, J.-M. Liu, and E. Dagotto, Phys. Rev. B **84**, 155117 (2011).
[6] J. D. Burton and E. Y. Tsymbal, Phys. Rev. B **80**, 174406 (2009).
[7] K. F. Wang, J.-M. Liu, and Z. F. Ren, Adv. Phys. **58**, 321 (2009).
[8] C. A. F. Vaz, J. Hoffman, C. H. Ahn, and R. Ramesh, Adv. Mater. **22**, 2900 (2010).
[9] W. Eerenstein, N. D. Mathur, and J. F. Scott, Nature (London) **442**, 760 (2006).
[10] K. L. Livesey, Phys. Rev. B **83**, 224420 (2011).
[11] X. Lu, Y. Kim, S. Goetze, X. Li, S. Dong, P. Werner, M. Alexe, and D. Hesse, Nano Lett. **11**, 3202 (2011).
[12] T.-H. Wang, C.-S. Tu1, H.-Y. Chen, Y. Ding, T. C. Lin, Y.-D. Yao, V. H. Schmidt, and K.-T. Wu, J. Appl. Phys. **109**, 044101 (2011).
[13] N. Biškup, A. de Andrés, N. M. Nemes, M. García-Hernandez, K. V. Glazyrin, and Y. M. Mukovskii, Appl. Phys. Lett. **90**, 222502 (2007).
[14] Z. Li, Y. Wang, Y. Lin, and C. Nan, Phys. Rev. B **79**, 180406(R) (2009).
[15] F. Y. Bruno, J. Garcia-Barriocanal, M. Varela, N. M. Nemes, P. Thakur, J. C. Cezar, N. B. Brookes, A. Rivera-Calzada, M. Garcia-Hernandez, C. Leon, S. Okamoto, S. J. Pennycook, and J. Santamaria, Phys. Rev. Lett. **106**, 147205 (2011).
[16] W. Eerenstein, M. Wiora, J. L. Prieto, J. F. Scott, and N. D. Mathur, Nat. Mater. **6**, 348 (2007).
[17] X. Moya, E. Stern-Taulats, S. Crossley, D. González-Alonso, S. Kar-Narayan, A. Planes, L. Mañosa, and N. D. Mathur, Adv. Mater. **25**, 1360 (2013).
[18] C. Thiele, K. Dörr, O. Bilani, J. Rödel, and L. Schultz, Phys. Rev. B **75**, 054408 (2007).
[19] C. A. F. Vaz, J. Hoffman, A. B. Posadas, and C. H. Ahn, Appl. Phys. Lett. **94**, 022504 (2009).
[20] C. A. F. Vaz, J. Phys.: Condens. Matter **24**, 333201 (2012).

[21] A. Alberca, N. M. Nemes, F. J. Mompean, N. Biskup, A. de Andres, C. Munuera, J. Tornos, C. Leon, A. Hernando, P. Ferrer, G. R. Castro, J. Santamaria, and M. Garcia-Hernandez, Phys. Rev. B **84**, 134402 (2011).

[22] A. Alberca, C. Munuera, J. Tornos, F. J. Mompean, N. Biskup, A. Ruiz, N. M. Nemes, A. de Andres, C. León, J. Santamaría, and M. García-Hernández, Phys. Rev. B **86**, 144416 (2012).

[23] E. Dagotto, *Nanoscale Phase Separation and Colossal Magnetoresistance: The Physics of Manganites and Related Compounds* (Springer, Berlin, 2003), Vol. 136.

[24] F. Jona and G. Shirane, *Ferroelectric Crystals* (Pergamon Press, Oxford, 1962).

[25] G. H. Kwei, A. C. Lawson, S. J. L. Billinge, and S.-W. Cheong, J. Phys. Chem. **97**, 2368 (1993).

[26] H. Zheng, J. Wang, S. E. Lofland, Z. Ma, L. Mohaddes-Ardabili, T. Zhao, L. Salamanca-Riba, S. R. Shinde, S. B. Ogale, F. Bai, D. Viehland, Y. Jia, D. G. Schlom, M. Wuttig, A. Roytburd, and R. Ramesh, Science **303**, 661 (2004).

[27] P. Zheng, J. A. Bain, and M. H. Kryder, IEEE Trans. Magn. **31**, 2700 (1995).

[28] Corrugation in the STO tetragonal phase below 105 K implies a roughness of 4–9 Å: S. Singh, T.-Y. Chien, J. R. Guest, and M. R. Fitzsimmons, Phys. Rev. B **85**, 115450 (2012).

[29] P. Marton, I. Rychetsky, and J. Hlinka, Phys. Rev. B **81**, 144125 (2010).

[30] M. Harder, Z. X. Cao, Y. S. Gui, X. L. Fan, and C.-M. Hu, Phys. Rev. B **84**, 054423 (2011).

[31] M. Golosovsky, P. Monod, P. K. Muduli, and R. C. Budhani, Phys. Rev. B **85**, 184418 (2012).

[32] M. R. Fitzsimmons and C. F. Majkrzak, in *Modern Techniques for Characterizing Magnetic Materials*, edited by Y. Zhu (Kluwer, Boston, 2005), pp. 107–152.

[33] A. Hoffmann, S. G. E. te Velthuis, Z. Sefrioui, J. Santamaria, M. R. Fitzsimmons, S. Park, and M. Varela, Phys. Rev. B **72**, 140407(R) (2005).

[34] Yaohua Liu, C. Visani, N. M. Nemes, M. R. Fitzsimmons, L. Y. Zhu, J. Tornos, M. Garcia-Hernandez, M. Zhernenkov, A. Hoffmann, C. Leon, J. Santamaria, and S. G. E. te Velthuis, Phys. Rev. Lett. **108**, 207205 (2012).

[35] S. Park, M. R. Fitzsimmons, C. F. Majkrzak, B. D. Schultz, and C. J. Palmstrøm, J. Appl. Phys. **104**, 083905 (2008).

[36] S. Chikazumi, *Physics of Ferromagnetism,* 2nd ed. (Oxford University Press, Oxford, 2009), Vol. 94.

[37] N. M. Nemes, M. Garcia-Hernandez, Z. Szatmari, T. Feher, F. Simon, C. Visani, V. Pena, C. Miller, J. Garcia-Barriocanal, F. Bruno, Z. Sefrioui, C. Leon, and J. Santamaria, IEEE Trans. Magn. **44**, 2926 (2008).

[38] E. Du Trémolet de Lacheisserie, D. Gignoux, and M. Schlenker, in *Magnetism*, edited by E. du Trémolet de Lacheisserie, D. Gignoux, and M. Schlenker (Springer, Berlin, 2006) Vol. 1.

[39] E. Du Tremolet de Lacheisserie, *Magnetostriction: Theory and Applications of Magnetoelasticity* (CRC Press, Boca Raton, 1993).

[40] A. del Moral, *Handbook of Magnetostriction and Magnetostrictive Materials* (Del Moral Publisher, Zaragoza, Spain, 2008), Vol 1.

[41] C. A. F. Vaz, arXiv:0811.2146.

[42] J. O'Donnell, M. S. Rzchowski, J. N. Eckstein, and I. Bozovic, Appl. Phys. Lett. **72**, 1775 (1998).

[43] C.-R. Chang, Phys. Rev. B **48**, 15817 (1993).

[44] R. C. O'Handley and S.-W. Sun, J. Magn. Magn. Mater. **104–107**, 1717 (1992).

[45] E. du Tremolet de Lacheisserie and J. Rouchy, J. Magn. Magn. Mater. **28**, 77 (1982).

[46] C. Kittel and P. McEuen, *Introduction to Solid State Physics* (Wiley, New York, 1996).

[47] M. Ziese, Rep. Prog. Phys. **65**, 143 (2002).

[48] M. C. Martin, G. Shirane, Y. Endoh, K. Hirota, Y. Moritomo, and Y. Tokura, Phys. Rev. B **53**, 14285 (1996).

[49] A. J. Millis, Phys. Rev. B **55**, 6405 (1997).